International Journal of Non-Linear Mechanics 118 (2020) 103255

Contents lists available at ScienceDirect

International Journal of Non-Linear Mechanics

journal homepage: www.elsevier.com/locate/nlm

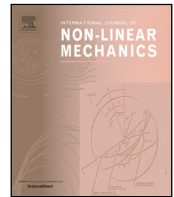

Feasibility study of a resonant accelerometer with bistable electrostatically actuated cantilever as a sensing element

Omer HaLevy *, Naftaly Krakover, Slava Krylov

School of Mechanical Engineering, Faculty of Engineering, Tel Aviv University, Ramat Aviv, Tel Aviv, 69978, Israel

ARTICLE INFO

Keywords:
MEMS
Bistable cantilever
Resonant accelerometer
Fringing electrostatic fields

ABSTRACT

We report on a feasibility study of a resonant accelerometer incorporating fringing electrostatic fields actuated cantilever serving as a sensing element. Device's dynamics are described using the reduced order (RO) Galerkin and numerical finite differences (FD) models, the finite elements (FE) analysis is used for the evaluation of the electrostatic forces. The architecture of the electrodes designed to be thicker than the cantilever allows tuning of the beam behavior in a wide range, starting from linear and up to bistable responses. By choosing an appropriate value of the actuating voltage close to the bistability threshold the cantilever can be positioned in the configuration where the frequency sensitivity of the device to the electrode's deflection is enhanced while the frequency itself is higher than in the initial inactuated state. In accordance with the model results, by integrating the bistable cantilever with a proof mass, it is possible to design a highly sensitive resonant accelerometer with the state of the art performance.

1. Introduction

Micro scale inertial sensors – accelerometers and angular rate sensors (micro gyros) – are probably the most common and commercially successful devices in the realm of a steadily growing microelectromechanical systems (MEMS) industry. Since the first batch-fabricated micro accelerometer was reported back in the seventies [1,2], inertial sensors remain among the most intensively researched and widely used micro scale devices. One of the promising approaches for performance enhancement of miniaturized mechanical sensors in general and accelerometers in particular is based on monitoring of the device spectral characteristics instead of a direct quasi-static displacement measurement.

In resonant sensors, the natural frequencies of the vibrating element are affected by the device parameters and environmental stimuli. By measuring the natural frequency of the device, the quantity of interest can be extracted [3]. For example, in mass sensors allowing detection of extremely small, down to attogram and even zeptogram, masses [4–6], the frequency of a vibrating structure decreases when a mass is attached to it. Frequency based sensing also lays the foundations of atomic force microscopy (AFM) [7], which is one of the most sensitive and well-established sensing technologies. The applicability of resonant sensing based on electromechanical micro- and nanodevices was explored in gas sensors [8], pressure sensors [9,10], electric/magnetic fields sensors and micro gyroscopes [11,12]. In micromechanical devices, resonant sensing has numerous advantages when compared to the direct analog quasi-static displacement detection. Dynamically operated devices distinguished by high frequencies and stiffness are less prone to the negative influence of environmental vibrations and mechanical shocks, demonstrate higher bandwidth and reduced Flicker ($1/f$) noise [13,14]. Since in the frequency-based sensors the vibrational amplitude itself is not the measured quantity and could be just above the detection limit [3,15], the requirements to the accuracy of the displacements detection are less demanding. Not less important, operation of the device at the smallest possible amplitudes improves the linearity of the sensor, eliminates undesired couplings and decreases power consumption.

In resonant sensors the shift in the device natural frequency occurs when a parameter to be measured alters either the stiffness or the mass of the structure [16,17]. In contrast to mass sensors [4–6], resonant accelerometers commonly exploit the dependence between the device's effective stiffness and the inertial (acceleration) loading resulting in a deflection of the proof mass [18–21]. Generally speaking, to achieve the situation when the stiffness is configuration-dependent, some kind of nonlinearity should be present in the system. Because MEMS devices, and, in particular, spring suspension elements, are in most cases fabricated from physically linear materials, such as silicon or quartz, the only way of introducing nonlinearity is through an appropriate structural design resulting in geometric nonlinearity. In this context, based on the type of nonlinearity, all resonant accelerometers could be subdivided into two groups: the devices based on mechanical stiffness/frequency tuning and those based on electrostatic stiffness tuning.

* Corresponding author.
E-mail address: omerlev1@mail.tau.ac.il (O. HaLevy).

https://doi.org/10.1016/j.ijnonlinmec.2019.103255
Received 9 May 2019; Received in revised form 1 August 2019; Accepted 13 August 2019
Available online 16 August 2019
0020-7462/© 2019 Elsevier Ltd. All rights reserved.

Among mechanically tuned devices, a dominant architecture is that of the vibrating beam accelerometer (VBA), which is one of the most sensitive devices implemented in high-end inertial instruments [18–21]. This device consists of one or several double-clamped resonating beams (ties) connected to a proof mass at one end and anchored at the other end. The frequency modulation is due to the axial force applied to the beam by the proof mass. To achieve detectable frequency shifts at small accelerations, force amplification approaches, realized either by leverage compliant mechanisms [19–23], or by designing appropriate in-plane [24,25], out-of-plane rotational [18,24,26–28] or linear movements [29], were suggested, at the expense of added design and fabrication complexities. A possible alternative is the use of the configuration-dependent electrostatic forces as the source of nonlinearity in inertial sensors [30–34]. In these devices, the decrease of the distance between the sensing element and the actuating electrode is accompanied by a softening effect and decrease in the resonant frequency. Electrostatically operated sensors are prone to the so-called pull-in instability, when the device collapses toward the electrode at the voltage exceeding certain critical value. On the one hand, the frequency to deflection sensitivity of the device increases when the structure approaches the pull-in point, which is a limit point of the voltage-deflection curve. On the other hand, presence of pull-in, which may result in an irreversible damage, such as electrical short with the electrode, stiction, or wear, limits the dynamics range of the sensor. Moreover, since the effective stiffness and the natural frequency of the device decrease when the vibrating structure is positioned closer to the pull-in point, the sensor's bandwidth is reduced. It is to say, there is a trade-off between the device sensitivity on the one side and bandwidth, dynamic range and reliability on the other side. For these reasons, the working point of the electrostatic resonant accelerometers is commonly chosen far enough from the pull-in point. Note that while close-loop feedback control can be used to eliminate pull-in and tailor the voltage-deflection characteristics [35,36], implementation of these techniques in the micro-scale sensors is not always suitable for practical purposes.

One of the approaches to avoid the pull-in related limitations is the use of curved bistable micro beams [37,38]. In these structures, able to stay in two different configurations at the same loading, the transition between the two states is through the snap-through buckling mechanism. Since snap-through is a limit point of the equilibrium curve, the frequency sensitivity is enhanced in the vicinity of the critical point [39,40]. But, in contrast to pull-in, the snap-through is reversible and is not accompanied by contact. Moreover, by choosing an appropriate geometry, the snap-through can be eliminated and replaced by an inflection point where the effective stiffness can be tailored to a desired value. The frequency-based displacement sensing using curved micro beams electrostatically coupled to a moving electrode was demonstrated in [41]. However, these devices, intrinsically based on a double-clamped beam architecture, have several major drawbacks, such as high sensitivity to residual and thermal stress [42,43] and to the initial geometry, which imposes challenging requirements to the fabrication accuracy.

Cantilevers, as opposed to double-clamped beams, are distinguished by low sensitivity to the residual stress and temperature and can be fabricated using established micro machining approaches. This explains their widespread use in resonant sensors [4,13,44,45]. However, since cantilevers are mechanically linear, they cannot be used without modification as a highly responsive sensing element in resonant accelerometers, perhaps except for the operation close to the pull-in point. One of the possibilities to overcome this limitation is the use of actuation by fringing electrostatic fields. It was previously shown [45–49] that for certain electrodes configurations, such as non-interdigitated comb electrodes [46] or vertical comb drives [47], the voltage-deflection characteristic can be non-monotonic and the device may exhibit bistability. Motivated by an attempt to combine the intrinsic advantages of cantilevers with frequency tuning and sensitivity enhancement abilities of bistable devices, a concept of a bistable cantilever actuated by fringing electrostatic fields was suggested and analyzed theoretically in [50]. The implementation of this architecture for pressure sensing was reported in [9]. An important feature of this device, along with its simplicity and robustness, is an ability to reach stiffening rather than softening behavior by applying the electrostatic force. In this case, the device effective stiffness and frequency both increase with actuating voltage. However, since in the devices reported in [9,50] the cantilever and the surrounding electrode were fabricated from the same structural layer, an additional force was necessary to bring the device to a working point, close to the highly sensitive snap-through configuration. This complicates the device design and operation and may require high actuation voltages.

In the present work we introduce an electrode configuration allowing positioning of the cantilever within the high sensitivity region already in the initial "as-fabricated state". As a result, no additional actuation is necessary to bring the device to the working point. The effect is achieved by designing the side electrode to be thicker than the cantilever. Moreover, the suggested architecture results in the hardening behavior of the device and allows to increase the effective natural frequency and consequently the bandwidth of the sensor in the vicinity of the working point. We present a generic model of a resonant accelerometer incorporating a vibrating cantilever interacting with the proof mass through fringing field electrostatic force. Model results demonstrate feasibility of the suggested approach.

2. Model of the cantilever actuated by fringing electrostatic field

2.1. Formulation

The device shown in Fig. 1(a) is a cantilever of the length L, width b and thickness d designed to deflect in the out-of-plane (z) direction. A side electrode of length L_S and thickness d_S is located at the distance g_S from the beam. In the initial, as-fabricated, state, the bottom surface of the beam is co-planar with the bottom surface of the side electrode. Hereafter this configuration is referred as the reference configuration. Since the side electrode is thicker than the beam the fringing field emerging from the electrode is not symmetric and is a source of the actuating electrostatic force F_{es} pulling the beam in the positive z-direction, toward the mid height of the side electrode. In the position corresponding to the mid height of the electrode, the field is symmetric, and the resultant electrostatic force is zero. Since the beam cannot be deflected in a negative z-direction, apart from the electrode, only by the electrostatic force, an additional actuation force F_M, referred hereafter as a "mechanical" force, is provided. With application of a steady DC voltage V_S to the side electrode and with F_M present, the beam reaches equilibrium configuration, Fig. 1(b).

In the framework of the Euler–Bernoulli model, under the small deflections assumptions, allowing to neglect the rotary inertia and the nonlinear curvature, the dynamics of the slender beam are governed by the equation

$$EI_{yy}\frac{\partial^4 \hat{w}}{\partial \hat{x}^4} + \rho A \frac{\partial^2 \hat{w}}{\partial \hat{t}^2} = -\hat{F}_M + V_S^2 \hat{F}_{es} H(\hat{x} - \hat{x}_S) \tag{1}$$

Here $\hat{w}(\hat{x},\hat{t})$ is the deflection of the cantilever in the positive z-direction, E and ρ are the elastic modulus and the mass density of the cantilever material, respectively, $A = bd$ and $I_{yy} = bd^3/12$ are the area and the second moment of area of the cantilever cross section, respectively. In addition, $\hat{F}_{es}(\hat{w})$ is the electrostatic force (per unit length and per unit voltage) associated with the fringing fields emerging from the side electrode, V_S is the voltage applied to the electrode, $H(\hat{x})$ is the Heaviside step function and $\hat{x}_S$ is the starting point coordinate of the side electrode. The prescribed, independent on the beam deflection, uniformly distributed mechanical actuation force $\hat{F}_M$ is positive when it acts in the negative z−direction.

We are interested in developing an expression for the frequencies of the free undamped vibrations around the equilibrium configuration. To this end we introduce a perturbation to the beam deflection and

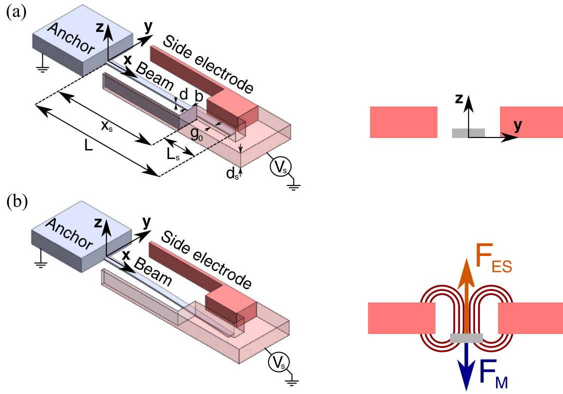

Fig. 1. (a) Schematics of the undeformed cantilever in the reference (as fabricated) configuration. (b) Deformed beam in the equilibrium configuration. When the steady dc voltage V_S is applied to the side electrode the electrostatic and "mechanical" actuation forces and the elastic restoring forces are equilibrated. The inset shows schematically the fringing field lines and the resultant electrostatic force. The side (fringing) electrode is depicted by the bright red color; the beam is shown in the gray color. (For interpretation of the references to color in this figure legend, the reader is referred to the web version of this article.)

Table 1
Non-dimensional quantities.

Definition	Description
$x = \hat{x}/L$	Axial coordinate
$w = \hat{w}/(2d_S)$	Deflection
$t = \hat{t}\sqrt{EI_{yy}/(\rho AL^4)}$	Time
$F_M = L^4\hat{F}_M/(2EId_S)$	Mechanical force
$F_{es} = L^4\hat{F}_{es}/(2EId_S)$	Electrostatic force

linearize the resulting equation in terms of perturbations. Specifically, we convert Eq. (1) into a non-dimensional form (the non-dimensional quantities used in the development are listed in Table 1) and then set $w(x,t) = w^*(x) + v(x,t)$, where $w^*(x)$ is the equilibrium deflection corresponding to the voltage V_S and $v(x,t)$ is the small time-dependent deflection (the perturbation). As a result, we obtain two equations

$$w^{*(IV)} = -F_M + V_S^2 F_{es}^* H\left(x - x_S\right) \tag{2}$$

$$v^{(IV)} - V_S^2 G v H\left(x - x_S\right) + \ddot{v} = 0 \tag{3}$$

where $F_{es}^* = F_{es}(w^*)$ is the non-dimensional electrostatic force in the equilibrium configuration and

$$G = G(w^*) = \frac{dF_{es}}{dw}\Big|_{w^*} \tag{4}$$

Nonlinear ordinary differential equation Eq. (2) describes the equilibrium of the beam under the electrostatic and mechanical forces, while linear partial differential equation Eq. (3) (with space-dependent stiffness coefficient) governs free undamped vibrations around the equilibrium. Hereafter the prime and the over dot denote derivatives with respect to the non-dimensional spatial coordinate x and non-dimensional time t, respectively.

2.2. Reduced order model

To build a RO model of the beam, we use the Galerkin approach limited to a single term approximation. The equilibrium $w^*(x)$ and the dynamic $v(x,t)$ deflections are approximated by the expressions

$$w^*(x) \approx q^*\psi(x), \qquad v(x,t) \approx q(t)\psi(x) \tag{5}$$

Here q^* is the generalized coordinate corresponding to the equilibrium state, $q(t)$ is the generalized amplitude and $\psi(x)$ is the fundamental mode of vibration of a cantilever used as the base function

$$\psi(x) = 0.367\left[\sin(\beta_1 x) - \sinh(\beta_1 x) - \frac{\sin(\beta_1) + \sinh(\beta_1)}{\cos(\beta_1) + \cosh(\beta_1)}\left[\cos(\beta_1 x) - \cosh(\beta_1 x)\right]\right] \tag{6}$$

where $\beta_1 = 1.8751$ is the cantilever fundamental eigenvalue [51]. Since the base function is normalized in such a way that $\psi(1) = 1$, q^* and $q(t)$ correspond to the (static and dynamic) endpoint deflections of the beam.

By performing the usual Galerkin procedure, we obtain the RO counterparts of Eqs. (2) and (3)

$$I_1 q^* - V_S^2 \int_{x_S}^1 \psi F_{es}^* \, dx = -I_3 F_M \tag{7}$$

$$I_2\ddot{q} + \left(I_1 - V_S^2 \int_{x_S}^1 \psi^2 G \, dx\right) q = 0 \tag{8}$$

where $F_{es}^* = F_{es}^*(q^*\psi)$, $G = G(q^*\psi)$ and

$$I_1 = \int_0^1 (\psi'')^2 \, dx = 3.089, \quad I_2 = \int_0^1 \psi^2 \, dx = 0.250, \quad I_3 = \int_0^1 \psi \, dx = 0.391 \tag{9}$$

Since the electrode is significantly shorter than the cantilever we replace in Eqs. (7) and (8) the base function $\psi(x)$ by its constant average only inside the expressions for the electrostatic force and its derivative, namely [49,52],

$$F_{es}^*(q^*\psi) \approx \bar{F}_{es}^* = F_{es}^*(q^* I_3^S / L_S) \qquad G(q^*\psi) \approx \bar{G} = G(q^* I_3^S / L_S) \tag{10}$$

As a result of this simplification we obtain

$$I_1 q^* - V_S^2 I_3^S \bar{F}_{es}^* = -I_3 F_M \tag{11}$$

$$I_2\ddot{q} + (I_1 - V_S^2 I_2^S \bar{G}) q = 0 \tag{12}$$

where

$$I_2^S = \int_{x_S}^1 \psi^2 \, dx, \qquad I_3^S = \int_{x_S}^1 \psi \, dx \tag{13}$$

In accordance with Eq. (12) the effective stiffness is parameterized by V_S. From Eq. (12) one can extract the frequency of free vibrations around the equilibrium

$$f = f_0\sqrt{1 - \frac{V_S^2 I_2^S \bar{G}}{\beta_1^4 I_2}} \tag{14}$$

where $f_0 = \beta_1^2/(2\pi)$ is the non-dimensional fundamental mode frequency of the unactuated beam (at zero V_S). Since the exact eigenfunction of the cantilever is used as the base function, $I_1/I_2 = \beta_1^4$.

We define several figures of merits to quantify the frequency sensitivity of the device. The sensitivity of the frequency to the beam's deflection is reflected by the non-dimensional relative SF_w and the dimensional $\widehat{SF}_w$ scale factors defined in the following way

$$SF_w = \frac{1}{f_0}\frac{df}{dq^*} = -\frac{V_S^2 I_2^S}{2\beta_1^2\sqrt{I_2\left[\beta_1^4 I_2 - V_S^2 I_2^S \bar{G}\right]}}\left(\frac{d\bar{G}}{dq^*}\right) \tag{15}$$

$$\widehat{SF}_w = \frac{d\hat{f}}{d\hat{w}_L^*} = \frac{1}{2d_S}\sqrt{\frac{EI_{yy}}{\rho AL^4}}\frac{df}{dq^*} = \frac{1}{2d_S}\hat{f}_0 SF_w \tag{16}$$

where $\hat{w}_L^* = \hat{w}^*(L)$ depends on V_S and is found as a solution of Eq. (11); $\hat{f}_0 = f_0\sqrt{EI_{yy}/(\rho AL^4)}$ is the dimensional fundamental mode frequency of the unloaded cantilever.

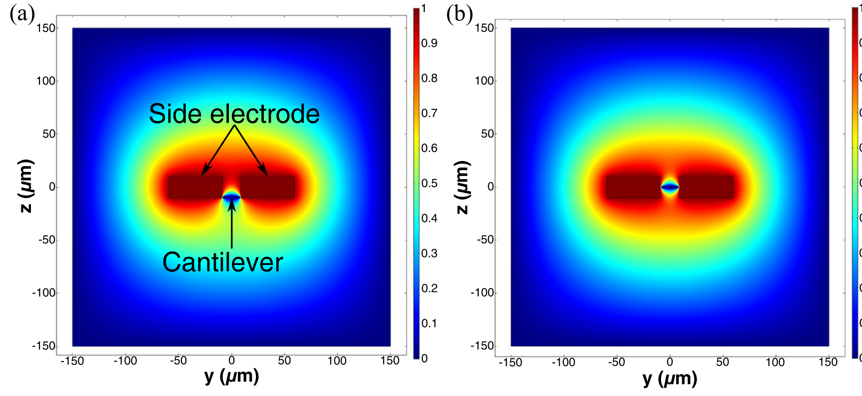

Fig. 2. Numerical results: the electric potential for different positions of the cantilever cross section with respect to the side electrode. (a) Zero displacement as defined in Fig. 1(a). (b) The beam is located at the middle of the side electrode. The geometric parameters are listed in Table 3, configuration A.

Table 2
Electrostatic force fitting coefficients. Parameters of the beam are in accordance with Table 3.

Coeff.	Value	Coeff.	Value
a_1	2.16×10^{-6} N/m	a_6	-3×10^{-6}
a_2	0	a_7	700000
a_3	375000	a_8	2.22×10^{-5}
a_4	10^{-6}	a_9	375000
a_5	700000	a_{10}	1.8×10^{-5}

Table 3
Material properties and geometric parameters of the device for three different configurations.

Configuration Parameter	A Value	B Value	C Value
L (μm)	150	270	420
b (μm)	16	16	16
d (μm)	1	2	3
L_S (μm)	37.5	68	105
d_S (μm)	20	40	50
g_S (μm)	1	2	3
V (V)	108	185	185
I_2^S		0.174	
I_3^S		0.207	
E (GPa)		170	
ρ (kgm^{-3})		2328	

2.3. Electrostatic force fitting

The electrostatic force acting on the beam was found numerically using the finite elements package COMSOL. A two-dimensional problem in terms of the electric potential was solved within a computational domain surrounding the beam and the electrodes. A generic cantilever cross section was placed at multiple vertical locations corresponding to the displacements between $\hat{z} = -0.5d_S$ and up to $\hat{z} = 1.5d_S$ with the increment of $0.04d_S$. For each beam position the resultant force was calculated. Fig. 2 shows the distribution of the electric potential for two differing beam positions. The geometric parameters b, g_S, d_S and d corresponded to those given in Table 3, configuration A. The boundary conditions corresponded to the zero voltage enforced on the beam and on the outer boundary of the computational domain and to the voltage of 1 V on the side electrode. After several successive mesh refinements carried out to assure convergence, the final adopted mesh included 27,800 elements and 126,100 degrees of freedom (DOF). The numerical data was imported into Maple [53] and the following fitting function was built

$$\hat{F}_{es} = a_1\phi(w) \qquad F_{es} = \gamma\phi(w) \tag{17}$$

$$\phi(w) = a_2 + \sum_{j=1}^{j=4}(-1)^{2j+1}\arctan\left(a_{2j+1}\left(w - a_{2j+2}\right)\right)$$

Here $a_i, i = 1 \ldots 10$ are fitting coefficients listed in Table 2, $\hat{F}_{es}$ and F_{es} are the dimensional and non-dimensional electrostatic force, respectively and $\gamma = L^4a_1/(2EId_S)$ is the electrostatic force coefficient. The non-dimensional electrostatic force obtained numerically, and the fit Eq. (17) are shown in Fig. 3.

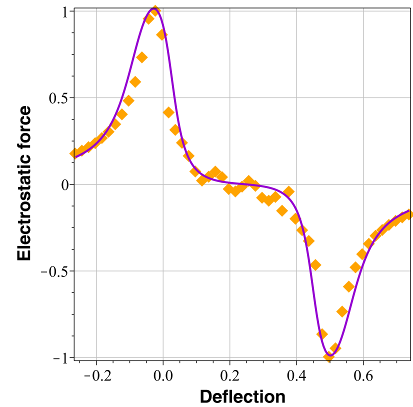

Fig. 3. Non-dimensional normalized electrostatic force per unit length of the beam calculated for a unit voltage applied on the side electrode: FE solution (markers) and fit, Eq. (17) (solid line).

2.4. Model results

The cantilever actuated by the fringing fields could be bistable [50]. In order to highlight the origin of the bistability in the case when the side electrode is thicker than the beam, we present the dependence between each of the forces acting on the beam (the elastic restoring and the electrostatic) and the cantilever's deflection. These forces are shown in Fig. 4(a) for the beam with the parameters detailed in Table 3, configuration A. In a certain range of the deflections where the elastic and the electrostatic forces have different signs and can equilibrate each other, the beam can be deflected solely by the electrostatic force. In contrast, in the intervals where the elastic and the electrostatic forces have the same sign, they are both restoring and the additional mechanical actuation force is necessary to bring the beam to the corresponding equilibrium configuration (see Eq. (11)).

The equilibrium curve of the beam is shown in Fig. 4(b). For low voltages the equilibrium curve is monotonic (the case of $V_S = 0$ and $V_S = 95$ V) whereas for higher V_S the snap-through (maximum) and release (minimum) limit points are observed indicating that the beam is bistable (the case of $V_S = 120$ V on the figure). While the bistability here is associated with the non-monotonic character of the electrostatic

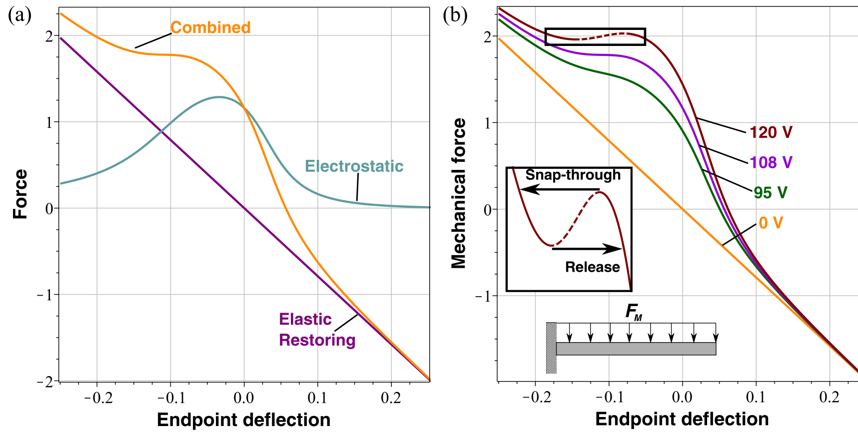

Fig. 4. (a) Forces acting on the beam: the linear elastic restoring force, the electrostatic fringing field force fit, Eq. (17) and the resultant sum of the elastic and the electrostatic forces. The side electrode voltage is $V_S = 108$ V. (b) Equilibrium curve for different values of the side electrode voltage V_S (numbers). Inset depicts the equilibrium curve zoom-in view in the vicinity of the snap-through and release instabilities, for $V_S = 120$ V. The parameters of the beam are listed in Table 3, configuration A.

force, Fig. 4(a), it appears due to the simultaneous contribution of the elastic restoring and the electrostatic forces and is not possible when one of the forces is absent. This is one of the distinguishing features of the device under consideration. The equilibrium curve corresponding to $V_S = 108$ V does not contain a snap-through point. Instead, there is an inflection point where the slope of the curve is close to zero. At this voltage the sensor can be operated in a continuous manner, without the jumps related to the snap-through collapse. Fig. 4 suggests that the bistability of the beam takes place at the deflections of the order of 0.1 of the electrode height. Consequently, only small (with respect to the beam length) deflections are required for the device functionality. For the beam with the parameters corresponding to the configuration A, Table 3 the maximal required deflection is of the order of $\pm 10\,\mu$m, which is much smaller than the beams length $L = 150\,\mu$m. As a result contribution of the nonlinear curvature, which in this case is smaller than approximately 0.67%, can be neglected.

It is instructive to find the bistability criterion, namely, the critical value of V_S corresponding to the bistability onset. Since the snap-through and the release are the limit points, the slope of the curve at these points is zero and the corresponding critical deflections can be found from the condition (see Eq. (11))

$$I_3 \frac{dF_M}{dq^*} = V_S^2 I_3^S \bar{G} - I_1 = 0 \tag{18}$$

The critical deflections and the corresponding values of F_M at the snap-through and the release points, as functions of V_S, are shown in Fig. 5. One observes that the bistability emerges at the voltages higher than a certain onset value. Due to the complexity of the fitting function, Eq. (17), the bistability onset value of V_S cannot be found in the closed form (as in the case of an initially curved double clamped bistable beam [37]) and a numerical solution of Eq. (18) is necessary. For the beam with the parameters detailed in Table 3, configuration A, the minimal value of the side electrode voltage required for bistability to occur was found to be $V_S^{min} = 109.2$ V.

It should be noted that along with the pull-in in the vertical z direction, additional stability loss scenarios could be anticipated. To assure that the voltages associated with these instabilities are higher than the operational values and do not interfere with the device functionality, we estimated critical voltages corresponding to two possible secondary pull-in cases. The first is the side pull-in associated with the cantilever's bending within the xy plane (see Fig. 1). The second scenario is the combined bending-torsion instability (lateral buckling of a thin walled cantilever, [54]). In both cases, while calculating the critical voltages, we took a conservative approach and considered the beam located at the mid height between the side electrode (as in Fig. 2(b)). In this configuration the electrostatic force is maximal. Since in our design the

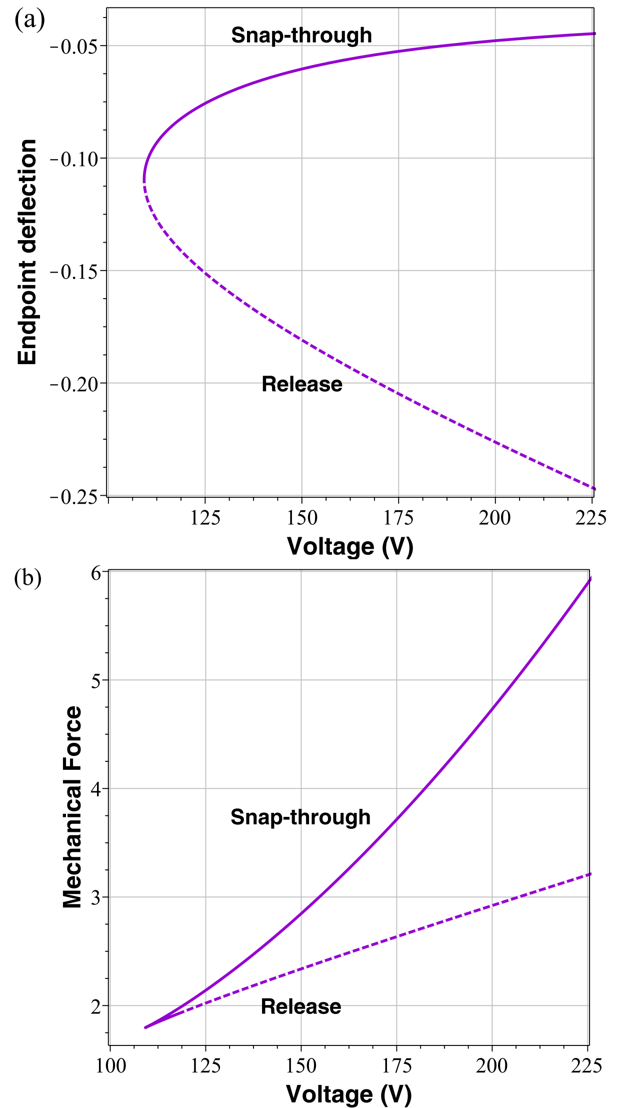

Fig. 5. (a) Critical (snap-through and release) endpoint deflections as the functions of the side electrode voltage V_S. (b) Critical mechanical forces as the function of V_S. Parameters of the beam are listed in Table 3, configuration A.

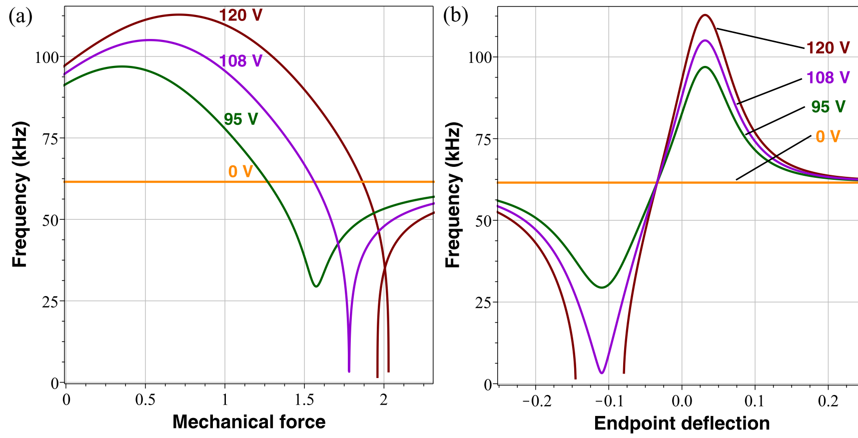

Fig. 6. Frequency of the free undamped vibrations around the equilibrium (a) as a function of the non-dimensional mechanical force F_M for different values of V_S (numbers) and (b) as a function of the beam non-dimensional endpoint deflection q^* for different values of V_S (numbers). The parameters of the beam are listed in Table 3, configuration A.

length of the side electrode L_S is smaller than that of the beam (see Table 3), we replaced the distributed electrostatic force by its resultant acting at the mid-length of the electrode. The electrostatic forces were calculated numerically, by fitting the results of the 2D finite elements solution (COMSOL), as described in Section 2.3. In the case of the in-plane side pull-in the electrostatic force provided by two electrodes was considered. In the case of the bending-torsion buckling the coarse conservative estimation was carried out by evaluating the electrostatic force provided by only one side electrode and by using the solution for the lateral buckling of a cantilever available in [54]. In both cases the critical pull-in voltages were found to be significantly higher than the maximal operational voltages presented in this work. For example, for a beam with dimensions corresponding to configuration A, Table 3, the in-plane side pull-in voltage was 344 V, while the critical voltage corresponding to the lateral (bending-torsion) pull-in was estimated to be 452 V.

The dependence between the frequencies of the free undamped vibrations around equilibrium and F_M is shown in Fig. 6 for different values of V_S. When no voltage is applied to the side electrode, the frequency sensitivity to the actuation force and to the beam deflection is zero. Increase of V_S results in the increase of the frequency/force (or frequency/deflection) curve slope and in higher sensitivity. Note that in accordance with Fig. 6, application of the voltage to the side electrode increases the effective stiffness and the natural frequency of the cantilever in the configurations close to the initial state, when the beam is located far away from the critical snap-through point. This situation is different from the common case of electrostatic softening, taking place when the device is operated by a gap-closing electrode. Since an arbitrarily low slope at the inflection point of the equilibrium curve, Fig. 4(b), can be tailored by applying an appropriate voltage, high frequency sensitivity combined with an acceptably high free vibrations frequency of the sensing element can be achieved, Fig. 6. We also note that there is a point corresponding to the non-dimensional deflection of $w^*(1) \approx -0.034$, where the frequency curves corresponding to different values of V_S coincide while the frequency itself is equal to the resonant frequency of the inactuated beam. This point is close to the maximum of the electrostatic force curve, Fig. 3, where the derivative of the electrostatic force with respect to deflection is zero. As a result, at this deflection the beam vibrates at its mechanical resonant frequency. Since that in this case the frequency is independent on the side electrode voltage, this configuration can serve as the calibration point for the sensor.

To investigate the influence of various parameters on the frequency and frequency sensitivity of the device, the numerical studies were carried out for three different configurations — A, B and C, Table 3. In all the cases, the length of the side electrode was $L_S = 0.25L$. Fig. 7(b) shows that as the structure becomes more slender, the frequency shift

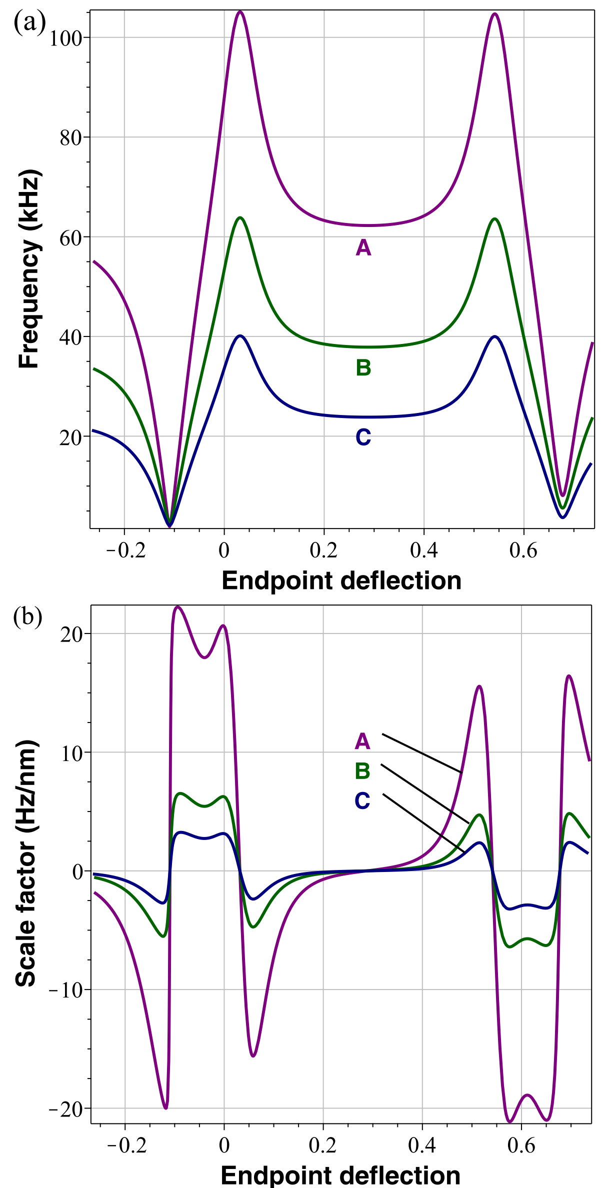

Fig. 7. Model results: (a) Frequency and (b) frequency sensitivity (scale factor $\widehat{SF}_w$), Eq. (16) as a function of the cantilever's non-dimensional endpoint deflection q^*, for three different configurations A, B and C listed in Table 3.

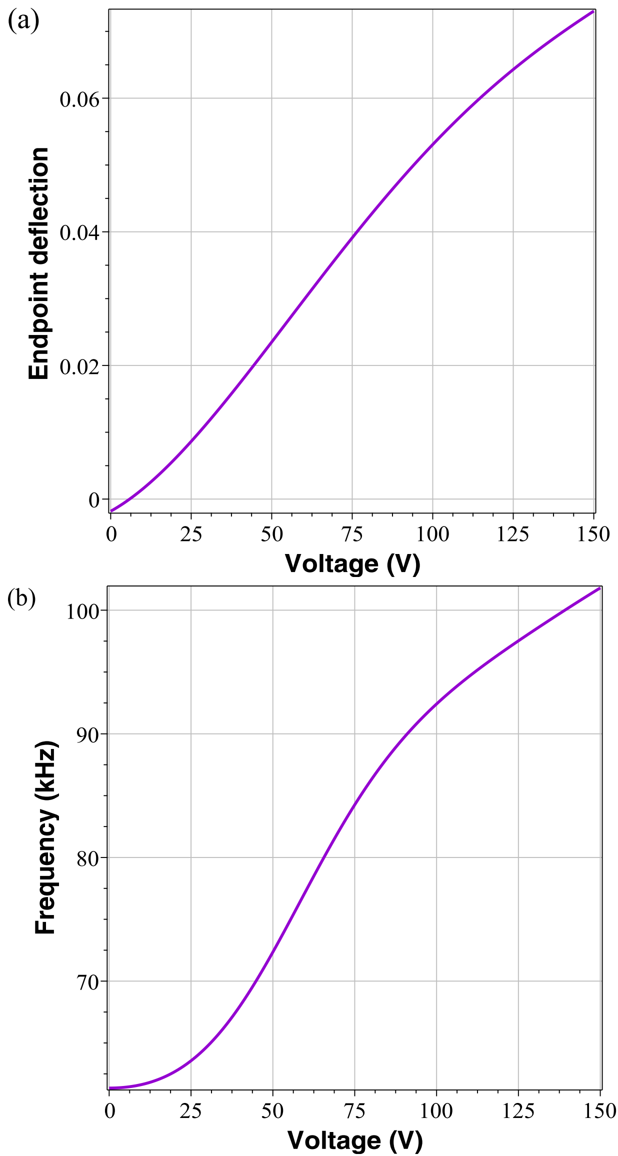

Fig. 8. (a) Equilibrium curve — non-dimensional deflection of the cantilever as the function of the DC voltage V_S applied to the side electrode and (b) frequency of free vibrations around the equilibria corresponding to the voltage V_S. No mechanical F_M or inertial (acceleration) forces are applied to the beam.

is more pronounced. In all three configurations the cantilever width b is the same. The ratio $\left(d/d_S\right) = \left(g_S/d_S\right) = (1/20)$ is also close to be identical in all the configurations. Reducing d_S, d and increasing the ratio $\left(b/g_S\right)$ leads to an improved SF_w. Fig. 7(b) shows that for the chosen beam's geometric parameters and the side electrode voltage value, the frequency is a continuous function of the endpoint deflection. Within a certain range of deflections, the frequency values become very small, close to zero. These deflections correspond to the configurations at the verge of bistability (at the limit point itself the frequency is zero). At the working point the frequency and SF should be maximized. According to Fig. 7, for configuration A, Table 3, if the equilibrium point is chosen close to the edge of the side electrodes, when $q^* = 0.05$ ($\hat{w} = 2\,\mu\text{m}$), the natural frequency at the equilibrium point is $\hat{f}^* \approx 99\,\text{kHz}$ $\left(\text{which corresponds to } \hat{f}^* \approx 1.61\hat{f}_0\right)$. The corresponding SF_w is $\approx -14.3\,\text{Hz/nm}$. This value is significantly higher than reported in [9] for a single layer fringing field actuated cantilever.

It is instructive also to consider the change of the linearized natural frequency of the beam as a function of the side electrode voltage in the case when no mechanical force is applied to the beam. To find the frequency of free linear vibrations around an equilibrium, the static deflections for each voltage was first found using Eq. (11) with $F_M = 0$. The resulting equilibrium curve is shown in Fig. 8(a). Then, the frequency for each voltage was calculated in accordance with Eq. (12). The resulting frequency curve shown in Fig. 8(b) indicates that the frequency of the device can be up-tuned in a wide range by applying the DC voltage to the side electrode.

2.5. Numerical validation

The results presented above are obtained using an approximate single degree of freedom RO model. Namely, the static responses of the beam are obtained using the nonlinear algebraic Eq. (11) whereas the frequency of the free vibrations around the equilibrium are calculated using the linearized ordinary differential equation, Eq. (12). In addition to the possible inaccuracies associated with the single term truncation of the Galerkin series, both Eq. (11) and (12) incorporate the simplifying approximation Eq. (10) of the distributed electrostatic force. Thus, to verify the model and estimate its accuracy, numerical analysis was exploited using several approaches. First, the nonlinear ordinary differential equation Eq. (2) describing the beam's equilibrium was solved numerically using a boundary value problem (BVP) solver (midpoint finite differences with a Richardson extrapolation) implemented in Maple package. A mesh with 2048 nodes was used. The beam was loaded by a linearly increasing mechanical force F_M while the voltage applied to the side electrode was held constant. In addition, a three-dimensional FE analysis of the beam was carried out using COMSOL Multiphysics package. The beam, considered as a three-dimensional elastic body, was meshed by 15,000 tetrahedron solid elements with second-order interpolation functions. The FE model contained 88,000 DOFs. The actuating mechanical force was distributed uniformly along the entire length of the beam. The electrostatic force distributed within the region between $x_S \leq x \leq L$ was realized as a prescribed nonlinear, deflection-dependent loading function provided by the fitting, Eq. (17), with $\hat{w}(\hat{x})$ being the spatial, coordinate dependent, deflection. The results are presented in Fig. 9, where the equilibrium curves are shown for multiple values of V_S. The comparison shows an excellent agreement between the numerical and RO model results. For example, the relative error in the snap-through value of $\hat{F}_M$ between the RO and FD model results is 0.47%, the difference between the FD and the FE solutions is 1.18%.

To estimate the accuracy of the single mode approximation used to evaluate the frequencies of free vibrations around equilibrium, the linear eigenvalue problem, Eq. (3), was solved numerically for multiple values of F_M and for several constant values of V_S. FD discretization (2048 nodes) was implemented to convert Eq. (3) into a system of algebraic equations and the eigenvalues of the associated matrix were obtained using Matlab eigenvalue solver. The equilibrium deflection $w^*(x)$ necessary to evaluate the space-dependent coefficient G in Eq. (3) was calculated by numerically solving Eq. (2) (BVP solver realized in Maple) for each of the 3000 increments of F_M. Fig. 10 presents the results obtained using both the single DOF RO and the FD models, for four different values of V_S. Good agreement between the results is observed.

3. Implementation in an accelerometer

One of the promising applications of the vibrating cantilever considered here is its implementation as a sensing element in an electrostatically tuned resonant accelerometer [32,33,41]. In the device considered in the present work the interaction between the proof mass and the sensing element is by means of the fringing electrostatic field. One of the possible generic architectures allowing realization of the suggested approach is illustrated in Fig. 11(a). The tilting-type proof mass is suspended by two elastic torsion axes. Four sensing cantilevers

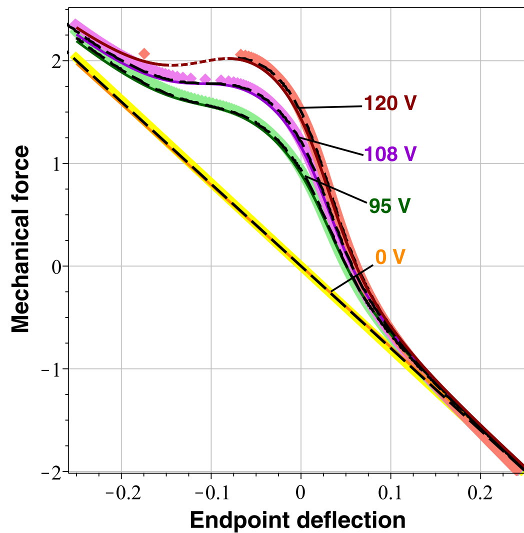

Fig. 9. Equilibrium curves dependence between the non-dimensional endpoint deflection and non-dimensional mechanical force for different values of the side electrode voltage V_S (numbers). Solid lines correspond to the single DOF RO model, Eq. (11) (see also Fig. 4). The black dashed lines are the results of the numerical FD solution of the BVP, Eq. (2). The diamonds markers correspond results of the three-dimensional FE analysis.

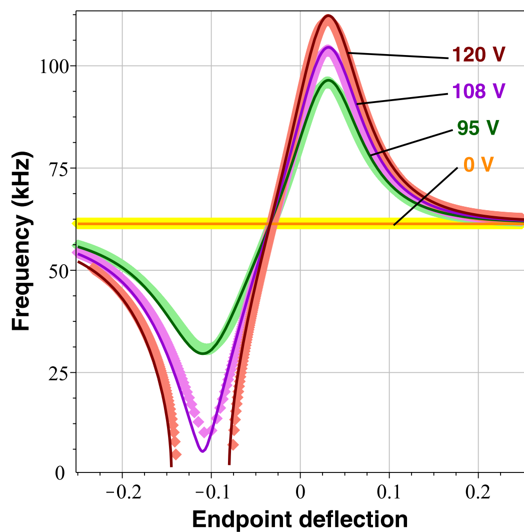

Fig. 10. Frequency of free vibrations around the equilibrium calculated for four different values of V_S (numbers). Solid lines correspond to the single DOF RO model Eq. (12), the diamonds markers represent the results of the finite difference solution of Eq. (3).

are positioned close to the corners of the mass, to provide an ability of differential measurement. The four openings in the mass (see an inset in Fig. 11), which is significantly thicker than the cantilevers, realizes the side electrodes geometry similar to shown in Fig. 1. Due to the offset between the mass center of gravity and the tilting axis, the presence of a vertical (z) acceleration results in a rotation of the mass, change in the relative position of the cantilevers with respect to the side electrode and therefore in the shift in the cantilever frequency. The geometry shown in Fig. 11(a) can be realized using several established fabrication processes. Here we assume that the mass and the cantilever are made of single crystal silicon using deep reactive ion etching (DRIE) and silicon on insulator (SOI) wafer as a starting material. The structural elements of different heights can be fabricated by using critically timed etching (e.g., see [55,56]). In this work, in order to explore the device

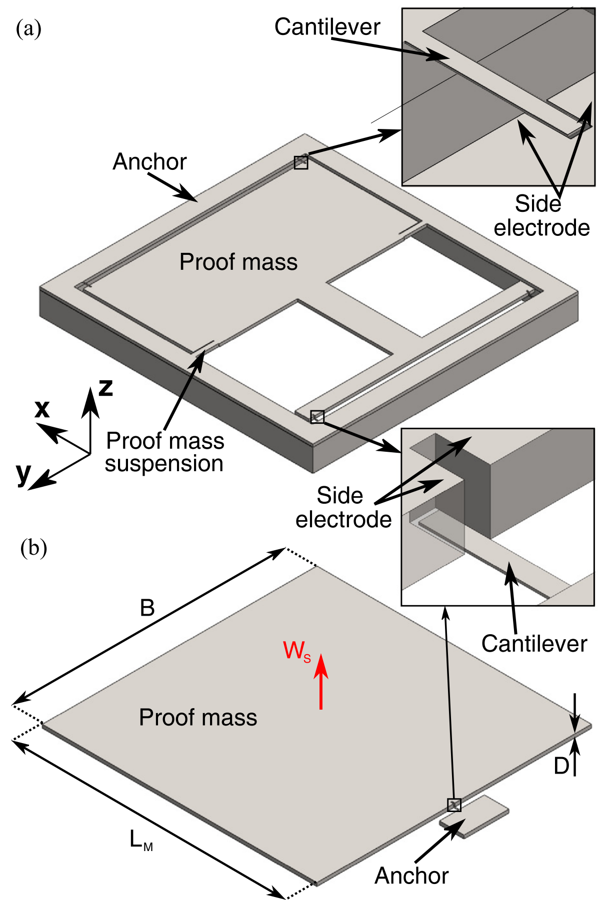

Fig. 11. (a) An artist rendering of a possible resonant accelerometer architecture showing a proof mass and four resonant sensing cantilevers. (b) A generic model of the accelerometer including a vertically moving proof mass and a single cantilever. The arrow W_S is in the positive deflection of the proof mass/side electrode deflection. Insets depict a zoom-in view of the cantilever and of the opening in the mass, serving as the side electrode.

feasibility and to estimate its performance, we considered a simplified generic model of a proof mass designed to deflect only in the vertical z direction. The mass interacts with the cantilever through the fringing electrostatic fields, as shown in Fig. 11(b).

While analyzing the behavior of the proof mass-cantilever system, we adopt several simplifying assumptions. First, since the beam vibrates at a frequency much higher than the proof mass fundamental mode frequency, we neglect the influence of the high-frequency component of the electrostatic interaction force on the mass response and consider only the quasi-static DC interactions. (Note, however, that in certain situations the high frequency forces may result in an appearance of effective steady components [57], which are neglected here as well.) Second, the large discrepancy between the natural frequencies of the mass and of the cantilever allows us to neglect the direct influence of the acceleration force on the cantilever deflection and to assume that the cantilever is actuated solely by the electrostatic force. This assumption is justified since the static deflection of accelerometers is generally inversely proportional to the mass frequency [51]. In contrast to the configuration investigated in Sections 2.1–2.4 here both the beam and the electrodes are movable. We consider the initial, as fabricated, configuration of the beam and of the electrodes as the reference configuration and adopt the clamping point of the cantilever (the anchor) as the reference for the vertical, out of plane, z deflection of the cantilever and of the electrodes. The positive absolute deflections of the cantilever and of the electrode are in the positive z-direction. The positive acceleration and the positive inertial force are in the negative

and positive z-directions, respectively. In this case, in accordance with Fig. 11, the positive acceleration results in the displacement of the electrode in the negative z-direction.

In view of the aforesaid, the equilibrium of the cantilever and of the electrode is described by the system of two equations

$$\begin{cases} EI\hat{W}^{*(IV)} = V_S^2 \hat{F}_{es} H\left(\hat{x}-\hat{x}_S\right) \\ k_M \hat{W}_S = -M\hat{a} - V_S^2 \int_0^L \hat{F}_{es} H\left(\hat{x}-\hat{x}_S\right) d\hat{x} \end{cases} \quad (19)$$

Here $\hat{W}_S$ and $\hat{W}^*(\hat{x})$ are the absolute deflections of the side electrode and of the beam, respectively, k_M is the stiffness of proof mass suspension, $M = \rho L_M DB$ is the mass; L_M, D and B are the length, height and width of the proof mass, respectively and $\hat{a}$ is the substrate acceleration. The electrostatic force $\hat{F}_{es} = \hat{F}_{es}(\hat{W}^* - \hat{W}_S)$ depends on the relative deflection of the beam with respect to the electrode

$$w^*(\hat{x}) = W^*(\hat{x}) - W_S \quad (20)$$

It is convenient to convert Eq. (19) into a non-dimensional form. In addition to the non-dimensional quantities defined in Table 1, we denote

$$W^* = \frac{\hat{W}^*}{2d_S}, \quad W_S^* = \frac{\hat{W}_S^*}{2d_S}, \quad \eta_M = \frac{EI_{yy}}{k_M L^3}$$
$$\gamma_a = \frac{Mg}{2d_S k_M} \quad \gamma = \frac{L^4 a_1}{2EI_{yy} d_S} \quad a = \frac{\hat{a}}{g} \quad (21)$$

We represent the absolute deflection of the beam using a single term approximation $W^* = Q^*\psi$ (where Q^* is the generalized coordinate corresponding to the non-dimensional absolute endpoint deflection of the beam), perform the usual Galerkin procedure and obtain

$$\begin{cases} Q^* I_1 = \gamma V_S^2 I_3^S \phi^* \\ W_S = -\gamma_a a - \eta_M \gamma V_S^2 \phi^* L_S \end{cases} \quad (22)$$

Here $\phi^* = \phi(Q^* I_3^S / L_S - W_S)$ is the nonlinear function of the deflections, Eq. (17). Note that Eq. (22) incorporates the approximation involving the replacement of the shape function $\psi(x)$ by its average value $\psi(x) \approx I_3^S / L_S$ inside ϕ^*. Eq. (22) is the system of two nonlinear algebraic equations with two unknowns Q^* and W_S. Using the first of Eqs. (22), $\gamma V_S^2 \phi^*$ can be eliminated from the second equation, providing the relation between the deflections of the electrode and of the beam

$$W_S = -\gamma_a a - \eta_M \frac{I_1}{I_3^S} L_S Q^* \quad (23)$$

Inserting W_S given by Eq. (23) into ϕ^* in the first of Eq. (22) yields the expression for the cantilever deflection at the equilibrium configuration

$$Q^* = \frac{\gamma V_S^2 I_3^S}{I_1} \phi^* \quad (24)$$

where now $\phi^* = \phi^*\left(\left(I_3^S / L_S + \eta_M I_1 L_S / I_3^S\right) Q^* + \gamma_a a\right)$ is expressed solely in terms of Q^*. Eq. (24), which is a nonlinear algebraic equation and can be solved only numerically, allows to find the absolute beam deflection Q^* for the given values of the side electrode voltage V_S and of the acceleration a. Once $Q^* = Q^*(V_S, a)$ is calculated, the relative deflection of the cantilever with respect to the electrode, which defines the electrostatic force, Eq. (17), can be evaluated by combining Eqs. (23) and (24)

$$q^* = Q^* - W_S = \frac{\gamma V_S^2 I_3^S}{I_1} \phi^* + \gamma_a a + \eta_M \frac{I_1}{I_3^S} L_S Q^* \quad (25)$$

It is convenient to approximate a functional dependence between the relative deflection q^* and the acceleration a using a polynomial fit limited to a third order

$$\tilde{q}^* = C_0 + C_1 a + C_2 a^2 + C_3 a^3 + C_4 a^4 \quad (26)$$

Here $C_i, i = 0..4$ are the fitting coefficients calculated for the specific system parameters and the specific V_S. The tilde above q^* is introduced to distinguish between the value q^* calculated directly from Eq. (25) and an approximate value $\tilde{q}^*$ given by a polynomial fit Eq. (26). The frequency of the cantilever in the presence of the acceleration can be found directly using Eq. (14) where q^* is replaced by the fit $\tilde{q}^*$, Eq. (26), namely

$$\hat{f}(a, V_S) = \hat{f}_0 \sqrt{1 - \frac{V_S^2 I_2^S \tilde{G}}{\beta_1^4 I_2}} \quad (27)$$

Here $\tilde{G} = G(\tilde{q}^* I_3^S / L_S)$ (see Eq. (10)) and G is defined by Eq. (4). We recall that $\hat{f}_0 = \beta_1^2/(2\pi)\sqrt{EI_{yy}/(\rho A L^4)}$ is the fundamental mode frequency of the unactuated beam.

One observes that the frequency depends on the acceleration. Consequently, it is possible to define two figures of merit to quantify the frequency sensitivity of the device. The (dimensional) sensitivity of the frequency to the mass (side electrode) displacement is

$$\widehat{SF}_{W_S} = \frac{d\hat{f}}{d\widehat{W}_S} \quad (28)$$

The sensitivity of the frequency to the acceleration is

$$\widehat{SF}_a = \frac{d\hat{f}}{da} = \frac{d\hat{f}}{d\tilde{q}^*}\frac{d\tilde{q}^*}{da}$$
$$= -\frac{f_0 V_S^2 I_2^S}{2\beta_1^2 \sqrt{I_2}\sqrt{\beta_1^4 I_2 - V_S^2 I_2^S \tilde{G}}} \left(\frac{d\tilde{G}}{d\tilde{q}^*}\right)\left(\frac{d\tilde{q}^*}{da}\right) \quad (29)$$

3.1. Device performance

To estimate the device performance calculations were carried out for the sensing cantilever with the parameters corresponding to the configuration A, Table 3. The adopted dimensions of the proof mass are listed in Table 4 and and are consistent with commonly found in realistic devices [27,29,58]. Since the device considered in this research is designed to operate in an open loop (the suggested frequency based sensing principle can be extended to the close loop operation as well), the stiffness parameters of the proof mass suspension were evaluated by setting the maximal mass deflection at the adopted maximal value of the acceleration and at zero V_S, namely

$$\hat{W}_S^{acc} = \frac{9.81 a_{\max} M}{k_M} \le \hat{W}_{max} \quad (30)$$

From this condition, the required stiffness and the natural frequency of the mass can be found

$$k_M = \frac{9.81 a_{\max} M}{\hat{W}_{max}}, \qquad \hat{f}_M = \frac{1}{2\pi}\sqrt{\frac{9.81 a_{\max}}{\hat{W}_{max}}} \quad (31)$$

For the adopted maximal acceleration of 40 g, we set $\hat{W}_{max} = 1$ μm, or, in the non-dimensional coordinates, $W_{max} = 0.025$. For the mass of the adopted dimensions and for the adopted deflection limitation, the natural frequency is $\hat{f}_M = 3153$ Hz. Now the stiffness of the suspension springs could be calculated (we neglect the influence of the electrostatic force while evaluating the mass stiffness parameters)

$$k_M = 4\pi^2 \hat{f}_M^2 M \quad (32)$$

Table 4
Material properties and geometric parameters of the proof mass.

Parameter	Value
L_M	4 mm
B	4 mm
D	20 μm
E	170 GPa
ρ	2328 kgm^{-3}
k_M	292 N/m
f_M	3153 Hz

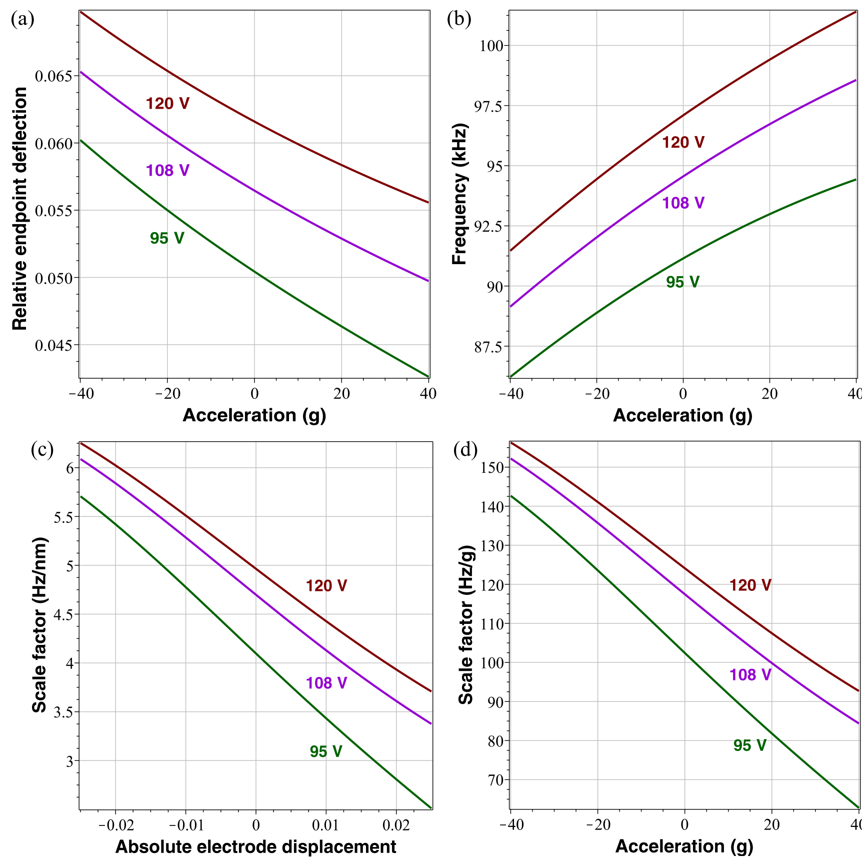

Fig. 12. Dependency of the system on the acceleration for system with the parameters defined in Table 3, configuration A and to Table 4 for different V_S (numbers). (a) Non-dimensional relative deflection q^* corresponding to the working point as a function of the acceleration. Acceleration is taken within a range such that Eq. (23) remains valid for the adopted configuration of the system. (b) Frequency of the cantilever (c) Frequency sensitivity per acceleration (the scale factor SF_a) (d) Frequency sensitivity per absolute mass displacement (the scale factor SF_{W_S}).

Table 5
Accelerometers sensitivity from the literature.

Reference	Sensitivity (Hz/g)	Resonant frequency (kHz)	Relative sensitivity (ppm/g)
H. Zhang et al. [59]	30	27	1035
C. Li et al. [60]	21	36.9	569
B. Li et al. [27]	15.7	35.3	445
Y. Wang et al. [61]	28.4	140.7	201
N. St. Michel [23]	91	20.3	4483
J. Zhang et al. [20]	250	22	11364
Le Traon et al. [18]	24	60	400
Y. Shang et al. [29]	584	64.9	8998
C. Comi et al. [33]	10	2.4	4167
H. Ding et al. [62]	61	548.4	111
B. Yang et al. [63]	52.6	2.8	18786
X. Zou and A.A. Seshia [64]	100	149.5	669
M. Aikele et al. [65]	70	400	175
This work — at $a = 0$ Mass freq. is $f_M = 1575\,\mathrm{Hz}$	667	82.6	8072

The dependence between the relative (with respect to the electrode bottom face) equilibrium deflection q^* of the beam and the acceleration is shown in Fig. 12(a). One observes that the non-dimensional and dimensional beam displacements through the whole range of accelerations of ± 40 g are $\Delta w^* \approx 0.015$ and $\Delta \hat{w}^* \approx 0.6$ μm, respectively. The scale factor curve, representing the dependence between the frequency of free undamped vibrations of the beam around the equilibrium point and the acceleration, is shown in Fig. 12(b). The frequency is calculated using Eq. (27) with the relative working point deflection $\tilde{q}^*$ approximated using the fit Eq. (26). The frequency to acceleration and frequency to mass displacement scale factors, obtained using Eqs. (28) and (29), respectively, are depicted in Figs. 12(d) and 12(c), respectively.

Our results suggest that for the adopted configuration relatively high, when compared to the reported results, Table 5, sensitivity of up to $\widehat{SF}_a \approx 152$ Hz/g, which corresponds to a relative sensitivity of ≈ 1700 ppm/g, can be achieved at ≈ -40 g. (It should be noted that the direct comparison of the device performance is difficult since the sensitivity depends on many factors such as the proof mass size and design, dynamic range of the accelerometer and resonance frequency of the mass and of the resonator. All these parameters are different in different sources.) The sensitivity in the configuration corresponding to zero acceleration is smaller and is $\widehat{SF}_a \approx 117$ Hz/g. This result suggests that, by introducing an initial offset between the cantilever and the mass, higher sensitivity at zero acceleration can be achieved. Fig. 13(a), (b) present the frequency and acceleration scale factor, respectively, as

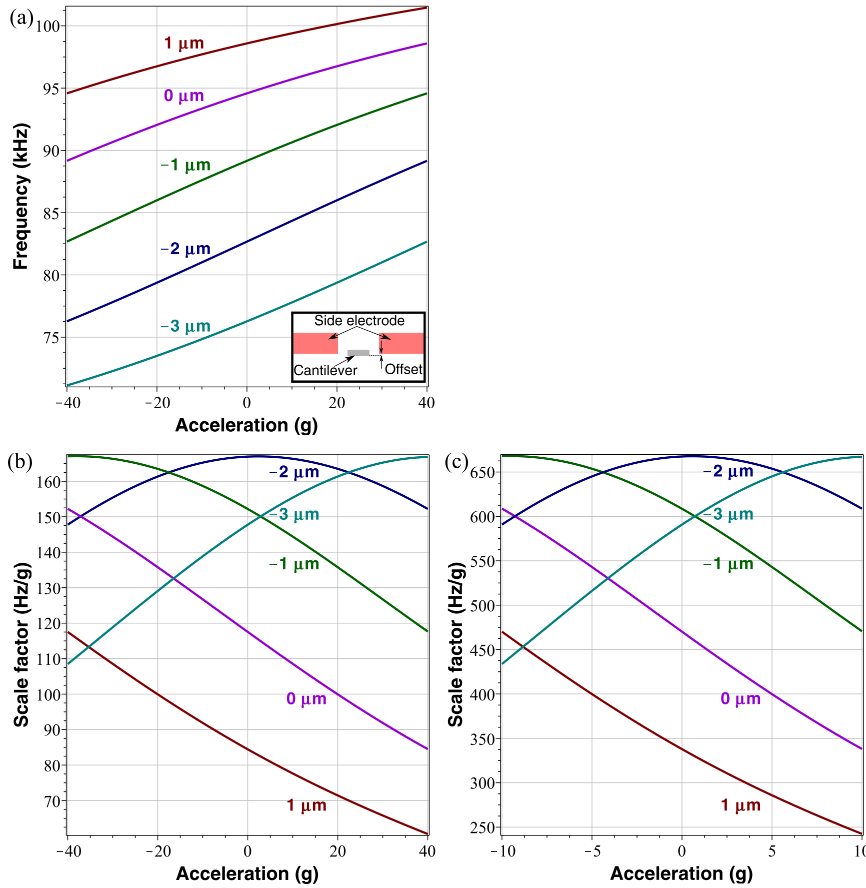

Fig. 13. Device performance for different initial offsets (numbers) between the proof mass and the cantilever. The parameters of the system are in accordance with Table 3, configuration A and Table 4. (a) Frequency of the cantilever. Inset depicts a positive initial offset between the side electrode and the cantilever (b) Frequency scale factor $\widehat{SF}_a$ (d) Frequency scale factor $\widehat{SF}_a$ for the reduced proof mass frequency of $f_M \approx 1575$ Hz.

a function of the acceleration, for $V_S = 108$ V and for different initial offsets. The offset values correspond to the proof mass position with respect to the initial, as fabricated, position of the cantilevers, when no acceleration nor voltage are applied, (see inset on Fig. 13(a)). For the initial offset of $-2\,\mu$m the maximum value for the scale factor is obtained at 0.6 g. For zero acceleration, the sensitivity is $\widehat{SF}_a \approx 167$ Hz/g. Another observation is that in the configuration corresponding to the maximal sensitivity the scale factor curve is close to linear, which is a beneficial feature in sensors. The main conclusion from these observation is that the best initial, as fabricated, configuration, where the maximal sensitivity could be achieved, corresponds to the positioning of the cantilever in such a way that its lower face is at the distance of ≈ 2 µm above the bottom surface of the side electrode. This could be achieved by fabricating the beam with an appropriate initial offset. Note in passing that by reducing the frequency of the proof mass from $\hat{f}_M = 3153$ Hz to ≈ 1575Hz, which is consistent with the values for high-end commercial accelerometers [58], the device sensitivity at zero acceleration can be increased to $\widehat{SF}_a \approx 667$ Hz/g (relative sensitivity of $\approx$ 8072 ppm/g), Fig. 13(c). Also, high end inertial sensors are typically operated in a close loop mode. In this context the cantilever strategically positioned in the location corresponding to the highest sensitivity and linearity of the scale factor are ideally suitable for the implementation in high end close loop accelerometers. While operated in the close loop mode, the position of the cantilever can be controlled rather than the position of the proof mass. The advantage is that the small size high frequency low absolute stiffness cantilever can be re-positioned using much smaller actuating voltage and in significantly shorter time.

4. Conclusions

The work is generally motivated by the development of high-end vibratory displacement or acceleration sensors based on resonant frequency monitoring of a micromechanical structure. The key component of the device is a vibrating cantilever actuated by fringing electrostatic fields. Due to the unique suggested architecture of the actuating electrodes, which are designed to be much thicker than the cantilever, the sensing beam may manifest bistability in the configuration close to its initial, "as fabricated", state. By applying the appropriate actuating voltage, the device's response can be strategically positioned at the verge of bistability, where the sensitivity of the resonant frequency to the cantilever deflections is enhanced. Specifically, when implemented as an accelerometer, the cantilever is positioned in a proximity of a proof mass whose displacements, caused by an inertial force, result in a perturbation of the fringing electrostatic fields and affect the cantilever's natural frequency. By monitoring the sensing cantilever resonant frequency, the acceleration is extracted. As opposed to the resonant devices operated by gap-closing electrodes and prone to pull-in instability, the snap-through collapse of the device suggested here is not accompanied by contact and is fully reversible. On the other hand, in contrast to the previously reported architectures based on the double clamped curved bistable beams, the suggested device is based on the cantilever architecture distinguished by low sensitivity to temperature and residual stress.

The feasibility study of the suggested sensing principle is carried out using the reduced order Galerkin model and the expected device performance is estimated. The fit of the nonlinear fringing-field electrostatic actuating force was built based on the results of the full-scale finite elements analysis of the electrostatic problem. The accuracy of

the approximate reduced order model was estimated through comparison with the results of the numerical finite differences solution of the governing equations. First, the beam frequency sensitivity to the deflections of the cantilever itself was investigated. In accordance with the model results, by appropriately choosing the working point (equilibrium) configuration, sensitivity of ≈ 20 Hz/nm can be achieved in the 150 μm long, 1 μm thick Si cantilever. The static response of the cantilever and consequently the working equilibrium configuration can be tailored by changing the steady DC voltage applied to the fringing fields electrodes. The developed bistability criterion, providing a critical value of the actuating voltage corresponding to the snap-through collapse, can serve as a useful tool for evaluation of the working point voltage. In contrast to the resonant sensors based on the electrostatic softening the working point frequency of the device considered in the present work is higher than the frequency in the initial unactuated configuration. This unique feature allows to avoid a trade off between the sensitivity and bandwidth commonly encountered in the bifurcation based sensors. A possibility of implementation in an accelerometer was explored as well using a generic model of a vibrating cantilever and a proof mass interacting though fringing electrostatic field. The model results show that high sensitivity of ≈ 160 Hz/g (for a $4\ \text{mm} \times 4\ \text{mm} \times 20\ \mu\text{m}$ Si proof mass with the frequency if 3153 Hz) and 6.5 Hz/nm can be achieved using the suggested architecture. By reduction of the proof mass frequency to 1575 Hz and by positioning the cantilevers in an appropriate location the device sensitivity of 667 Hz/g can be achieved. These numbers reflect the state-of-the-art performance in the realm of resonant accelerometers of this kind, Table 5.

Although the present work does not address fabrication, a remark should be made about possible influence of fabrication tolerances on the device performance. Specifically, the fabrication process may result in the appearance of horizontal (x or y directions, Fig. 1(a)) misalignment in the position of the beam between the electrodes. The misalignment in the x direction is effectively similar to the change of the electrode length L_S. Since $L_S \gg g_S$ and the dependence between the electrostatic force and L_S is linear, the x misalignment is less significant. To estimate the possible contribution of the lateral misalignment in the y direction we calculated numerically (2D finite elements, see Section 2.3) the electrostatic force in the z direction for the case when the distance between the beam and the right and the left electrodes are not identical. We found that for a misalignment of 10% of the electrostatic gap g_S the change in the out of plane electrostatic force is 5.7%. Due to an intrinsic tunability property of our device, the influence of the misalignment can be compensated by applying an appropriate DC voltage to the side electrodes. Note also that self-alignment fabrication process can be implemented, which will effectively eliminate misalignment [66].

To conclude, we believe that the suggested architecture and operational principle of the simple, manufacturable and potentially downscalable device can be implemented in other types of sensors such as force, mass and stress-based gas sensors.

Acknowledgment

The research is supported by the Israel Science Foundation (ISF, 383 grant no. 1272/16). The last author is supported by the Henry and Dinah Krongold Chair of Microelectronics, Israel.

References

[1] L.M. Roylance, J.B. Angell, A batch-fabricated silicon accelerometer, IEEE Trans. Electron Devices 26 (1979) 1911–1917.
[2] S.S. Chuang, Force Sensor using Double-Ended Tuning Fork Quartz Crystals, Technical Report, STATEK CORP ORANGE CA, 1983.
[3] P.S. Waggoner, H.G. Craighead, Micro-and nanomechanical sensors for environmental, chemical, and biological detection, Lab Chip 7 (2007) 1238–1255.
[4] B. Ilic, H. Craighead, S. Krylov, W. Senaratne, C. Ober, P. Neuzil, Attogram detection using nanoelectromechanical oscillators, J. Appl. Phys. 95 (2004) 3694–3703.
[5] K. Ekinci, Y. Yang, M. Roukes, Ultimate limits to inertial mass sensing based upon nanoelectromechanical systems, J. Appl. Phys. 95 (2004) 2682–2689.
[6] Y.-T. Yang, C. Callegari, X. Feng, K.L. Ekinci, M.L. Roukes, Zeptogram-scale nanomechanical mass sensing, Nano Lett. 6 (2006) 583–586.
[7] T. Albrecht, P. Grütter, D. Horne, D. Rugar, Frequency modulation detection using high-Q cantilevers for enhanced force microscope sensitivity, J. Appl. Phys. 69 (1991) 668–673.
[8] D.J. Joe, Y. Linzon, V.P. Adiga, R.A. Barton, M. Kim, B. Ilic, S. Krylov, J.M. Parpia, H.G. Craighead, Stress-based resonant volatile gas microsensor operated near the critically buckled state, J. Appl. Phys. 111 (2012) 104517.
[9] N. Krakover, B.R. Hic, S. Krylov, Resonant pressure sensing using a micromechanical cantilever actuated by fringing electrostatic fields, in: Micro Electro Mechanical Systems, MEMS, 2018 IEEE, IEEE, 2018, pp. 846–849.
[10] A.Z. Hajjaj, N. Alcheikh, M.A.A. Hafiz, S. Ilyas, M.I. Younis, A scalable pressure sensor based on an electrothermally and electrostatically operated resonator, Appl. Phys. Lett. 111 (2017) 223503.
[11] F.-x. Boillot, R. Laoubi, MEMS-sensor, Google Patents, 2018 US Patent 9, 856, 133.
[12] D.V. Dao, T. Toriyama, S. Sugiyama, Noise and frequency analyses of a miniaturized 3-dof accelerometer utilizing silicon nanowire piezoresistors, in: Sensors, 2004 Proceedings of IEEE, IEEE, 2004, pp. 1464–1467.
[13] M. Li, H.X. Tang, M.L. Roukes, Ultra-sensitive NEMS-based cantilevers for sensing, scanned probe and very high-frequency applications, Nature Nanotechnol. 2 (2007) 114.
[14] M. Li, A. Matyushov, C. Dong, H. Chen, H. Lin, T. Nan, Z. Qian, M. Rinaldi, Y. Lin, N.X. Sun, Ultra-sensitive NEMS magnetoelectric sensor for picotesla DC magnetic field detection, Appl. Phys. Lett. 110 (2017) 143510.
[15] T.E. Schäffer, H. Fuchs, Optimized detection of normal vibration modes of atomic force microscope cantilevers with the optical beam deflection method, J. Appl. Phys. 97 (2005) 083524.
[16] N. Maluf, K. Williams, Introduction to Microelectromechanical Systems Engineering, Artech House, 2004.
[17] S. Beeby, G. Ensel, M. Kraft, MEMS Mechanical Sensors, Artech House, 2004.
[18] O. Le Traon, D. Janiaud, J. Guerard, R. Levy, S. Masson, O. Ducloux, M. Pernice, R. Taibi, The fairy world of quartz vibrating mems, in: European Frequency and Time Forum, EFTF, 2012, IEEE, 2012, pp. 214–220.
[19] O. Lefort, S. Jaud, R. Quer, A. Milesi, Inertial grade silicon vibrating beam accelerometer, in: Inertial Sensors and Systems 2012. 6th Annual Conference. September 18–19, 2012. Karlsruhe, Germany, Karlsruhe Institute of Technology (KIT), 2012.
[20] J. Zhang, Y. Su, Q. Shi, A.-P. Qiu, Microelectromechanical resonant accelerometer designed with a high sensitivity, Sensors 15 (2015) 30293–30310.
[21] G. Xia, Y. Zhao, J. Zhao, Q. Shi, A. Qiu, Silicon vibrating beam accelerometer with ppm grade scale factor stability and tens-ppm grade full-range nonlinearity, in: Inertial Sensors and Systems, 2016 IEEE International Symposium on, IEEE, 2016, pp. 117–118.
[22] T.A. Roessig, R.T. Howe, A.P. Pisano, J.H. Smith, Surface-micromachined resonant accelerometer, in: Solid State Sensors and Actuators, 1997. TRANSDUCERS'97 Chicago., 1997 International Conference on, vol. 2, IEEE, 1997, pp. 859–862.
[23] N.A. St Michel, Force Multiplier in a Microelectromechanical Silicon Oscillating Accelerometer (Ph.D. thesis), Massachusetts Institute of Technology, 2000.
[24] P.H. Lafond, Modeling for error reduction in vibrating beam accelerometers, in: Position Location and Navigation Symposium, 1992. Record. 500 Years After Columbus-Navigation Challenges of Tomorrow. IEEE PLANS'92., IEEE, IEEE, 1992, pp. 126–132.
[25] W.C. Albert, Monolithic quartz structure vibrating beam accelerometer (VBA), in: Frequency Control Symposium, 1994. 48th., Proceedings of the 1994 IEEE International, IEEE, 1994, pp. 415–420.
[26] C. Burrer, J. Esteve, E. Lora -Tamayo, Resonant silicon accelerometers in bulk micromachining technology-an approach, J. Microelectromech. Syst. 5 (1996) 122–130.
[27] B. Li, Y. Zhao, C. Li, R. Cheng, D. Sun, S. Wang, A differential resonant accelerometer with low cross-interference and temperature drift, Sensors 17 (2017) 178.
[28] D.D. Shin, C.H. Ahn, Y. Chen, D.L. Christensen, I.B. Flader, T.W. Kenny, Environmentally robust differential resonant accelerometer in a wafer-scale encapsulation process, in: Micro Electro Mechanical Systems, MEMS, 2017 IEEE 30th International Conference on, IEEE, 2017, pp. 17–20.
[29] Y. Shang, J. Wang, S. Tu, L. Liu, D. Chen, Z-axis differential silicon-on-insulator resonant accelerometer with high sensitivity, Micro Nano Lett. 6 (2011) 519–522.
[30] S. Sung, J.G. Lee, B. Lee, T. Kang, Design and performance test of an oscillation loop for a MEMS resonant accelerometer, J. Micromech. Microeng. 13 (2003) 246.
[31] B.-L. Lee, C.-h. Oh, S. Lee, Y.-S. Oh, K.-j. Chun, A vacuum packaged differential resonant accelerometer using gap sensitive electrostatic stiffness changing effect, in: Micro Electro Mechanical Systems, 2000. MEMS 2000. the Thirteenth Annual International Conference on, IEEE, 2000, pp. 352–357.

[32] C. Comi, A. Corigliano, A. Ghisi, S. Zerbini, A resonant micro accelerometer based on electrostatic stiffness variation, Meccanica 48 (2013) 1893–1900.
[33] C. Comi, A. Corigliano, G. Langfelder, V. Zega, S. Zerbini, Sensitivity and temperature behavior of a novel z-axis differential resonant micro accelerometer, J. Micromech. Microeng. 26 (2016) 035006.
[34] C.R. Marra, F.M. Ferrari, S. Karman, A. Tocchio, F. Rizzini, G. Langfelder, Single-resonator, time-switched fm mems accelerometer with theoretical offset drift complete cancellation, in: 2018 IEEE Micro Electro Mechanical Systems, MEMS, IEEE, 2018, pp. 117–120.
[35] J.I. Seeger, B.E. Boser, Dynamics and control of parallel-plate actuators beyond the electrostatic instability, in: Transducers, vol. 99, 1999, pp. 474–477.
[36] S. Towfighian, G. Heppler, E. Abdel-Rahman, Analysis of a chaotic electrostatic micro-oscillator, J. Comput. Nonlinear Dyn. 6 (2011) 011001.
[37] S. Krylov, B.R. Ilic, D. Schreiber, S. Seretensky, H. Craighead, The pull-in behavior of electrostatically actuated bistable microstructures, J. Micromech. Microeng. 18 (2008) 055026.
[38] M.I. Younis, MEMS Linear and Nonlinear Statics and Dynamics, volume 20, Springer Science & Business Media, 2011.
[39] S. Krylov, N. Dick, Dynamic stability of electrostatically actuated initially curved shallow micro beams, Contin. Mech. Thermodyn. 22 (2010) 445–468.
[40] H.M. Ouakad, M.I. Younis, The dynamic behavior of MEMS arch resonators actuated electrically, Int. J. Non-Linear Mech. 45 (2010) 704–713.
[41] N. Krakover, B.R. Ilic, S. Krylov, Displacement sensing based on resonant frequency monitoring of electrostatically actuated curved micro beams, J. Micromech. Microeng. 26 (2016) 115006.
[42] A.M. Bataineh, M.I. Younis, Dynamics of a clamped–clamped microbeam resonator considering fabrication imperfections, Microsyst. Technol. 21 (2015) 2425–2434.
[43] S.A. Tella, A.Z. Hajjaj, M.I. Younis, The effects of initial rise and axial loads on MEMS arches, J. Vib. Acoust. 139 (2017) 040905.
[44] J. Tamayo, D. Ramos, J. Mertens, M. Calleja, Effect of the adsorbate stiffness on the resonance response of microcantilever sensors, Appl. Phys. Lett. 89 (2006) 224104.
[45] J. Small, W. Irshad, A. Fruehling, A. Garg, X. Liu, D. Peroulis, Electrostatic fringing-field actuation for pull-in free RF-MEMS analogue tunable resonators, J. Micromech. Microeng. 22 (2012) 095004.
[46] S.G. Adams, F.M. Bertsch, K.A. Shaw, N.C. MacDonald, Independent tuning of linear and nonlinear stiffness coefficients [actuators], J. Microelectromech. Syst. 7 (1998) 172–180.
[47] D. Hah, P.R. Patterson, H.D. Nguyen, H. Toshiyoshi, M.C. Wu, Theory and experiments of angular vertical comb-drive actuators for scanning micromirrors, IEEE J. Sel. Top. Quantum Electron. 10 (2004) 505–513.
[48] K.B. Lee, Non-contact electrostatic microactuator using slit structures: theory and a preliminary test, J. Micromech. Microeng. 17 (2007) 2186.
[49] S. Krylov, B.R. Ilic, S. Lulinsky, Bistability of curved microbeams actuated by fringing electrostatic fields, Nonlinear Dynam. 66 (2011) 403.
[50] N. Krakover, S. Krylov, Bistable cantilevers actuated by fringing electrostatic fields, J. Vib. Acoust. 139 (2017) 040908.
[51] L. Meirovitch, Elements of Vibration Analysis, McGraw-Hill, 1975.
[52] Y. Linzon, B. Ilic, S. Lulinsky, S. Krylov, Efficient parametric excitation of silicon-on-insulator microcantilever beams by fringing electrostatic fields, J. Appl. Phys. 113 (2013) 163508.
[53] M.U. Manual, Maplesoft, Waterloo Maple Inc, 2005.
[54] S.P. Timoshenko, J.M. Gere, Theory of Elastic Stability, Courier Corporation, 2009.
[55] N.M. Elman, S. Krylov, M. Sternheim, Y. Shacham-Diamand, Multiple aspect-ratio structural integration in single crystal silicon (MASIS) for fabrication of transmissive MOEMS modulators, Microsyst. Technol. 14 (2008) 287–293.
[56] S. Krylov, N. Molinazzi, T. Shmilovich, U. Pomerantz, S. Lulinsky, Parametric excitation of flexural vibrations of micro beams by fringing electrostatic fields, in: ASME 2010 International Design Engineering Technical Conferences and Computers and Information in Engineering Conference, American Society of Mechanical Engineers, 2010, pp. 601–611.
[57] I.I. Blekhman, Vibrational Mechanics: Nonlinear Dynamic Effects, General Approach, Applications, World Scientific, 2000.
[58] Colibrys, Ms1000 - datasheet, 2018, [Online], https://www.colibrys.com/wp-content/uploads/2016/12/30s-ms1000-e-04-18-datasheet.pdf.
[59] H. Zhang, B. Li, W. Yuan, M. Kraft, H. Chang, An acceleration sensing method based on the mode localization of weakly coupled resonators, J. Microelectromech. Syst. 25 (2016) 286–296.
[60] C. Li, Y. Zhao, R. Cheng, Z. Yu, Y. Liu, A resonant sensor composed of quartz double ended tuning fork and silicon substrate for digital acceleration measurement, Rev. Sci. Instrum. 85 (2014) 035004.
[61] Y. Wang, H. Ding, X. Le, W. Wang, J. Xie, A MEMS piezoelectric in-plane resonant accelerometer based on aluminum nitride with two-stage microleverage mechanism, Sensors Actuators A 254 (2017) 126–133.
[62] H. Ding, W. Wang, B.-F. Ju, J. Xie, A MEMS resonant accelerometer with sensitivity enhancement and adjustment mechanisms, J. Micromech. Microeng. 27 (2017) 115010.
[63] B. Yang, H. Zhao, B. Dai, X. Liu, A new silicon biaxial decoupled resonant micro-accelerometer, Microsyst. Technol. 21 (2015) 109–115.
[64] X. Zou, A.A. Seshia, A high-resolution resonant mems accelerometer, in: Solid-State Sensors, Actuators and Microsystems, TRANSDUCERS, 2015 Transducers-2015 18th International Conference on, IEEE, 2015, pp. 1247–1250.
[65] M. Aikele, K. Bauer, W. Ficker, F. Neubauer, U. Prechtel, J. Schalk, H. Seidel, Resonant accelerometer with self-test, Sensors Actuators A 92 (2001) 161–167.
[66] Y. Mizoguchi, M. Esashi, Design and fabrication of a pure-rotation microscanner with self-aligned electrostatic vertical combdrives in double SOI wafer, in: The 13th International Conference on Solid-State Sensors, Actuators and Microsystems, 2005. Digest of Technical Papers. TRANSDUCERS'05, volume 1, IEEE, 2005, pp. 65–68.